Pressure-induced superconductivity in $Bi_{2-x}Sb_xTe_{3-y}Se_y$

Tong He,[1] Xiaofan Yang,[1] Tomoya Taguchi,[1] Teppei Ueno,[1] Kaya Kobayashi,[1] Jun Akimitsu,[1] Hitoshi Yamaoka,[2] Hirofumi Ishii,[3] Yen-Fa Liao,[3] Hiromi Ota,[4] Hidenori Goto,[1] Ritsuko Eguchi,[1] Kensei Terashima,[1] Takayoshi Yokoya,[1] Harald O. Jeschke,[1] Xianxin Wu,[5] and Yoshihiro Kubozono[1,*]

[1]*Research Institute for Interdisciplinary Science, Okayama University, Okayama 700–8530, Japan*
[2]*RIKEN SPring-8 Center, Hyogo 679–5148, Japan*
[3]*National Synchrotron Radiation Research Center, Hsinchu 30076, Taiwan*
[4]*Advanced Science Research Center, Okayama University, Okayama 700–8530, Japan*
[5]*Institute for Theoretical Physics and Astrophysics, University of Würzburg, 97074 Würzburg, Germany*

(Received 9 May 2019; revised manuscript received 16 August 2019; published 19 September 2019)

We systematically investigated the pressure dependence of electrical transport and the crystal structure of topological insulator, $Bi_{2-x}Sb_xTe_{3-y}Se_y$, which showed no superconductivity down to 2.0 K at ambient pressure. The $Bi_{2-x}Sb_xTe_{3-y}Se_y$ crystal showed two structural phase transitions under pressure, from rhombohedral structure (space group No. 166, $R\bar{3}m$, termed phase I) to monoclinic structure (space group No. 12, $C2/m$, termed phase II), and from phase II to another monoclinic structure (space group No. 12, $C2/m$, termed phase III). Superconductivity appeared when applying pressure; actually the superconductivity of all $Bi_{2-x}Sb_xTe_{3-y}Se_y$ samples emerged in phase I. The superconducting transition temperature, T_c, increased against pressure in a pressure range of 0–15 GPa for all $Bi_{2-x}Sb_xTe_{3-y}Se_y$ samples, and the maximum T_c was 5.45 K, recorded at 13.5 GPa in $Bi_{2-x}Sb_xTe_{3-y}Se_y$ at $x = 0$ and $y = 1.0$. The magnetic field (H) dependence of the R–T plot for $Bi_{2-x}Sb_xTe_{3-y}Se_y$ was measured to characterize the superconducting pairing mechanism of pressure-induced superconducting phase.

DOI: 10.1103/PhysRevB.100.094525

I. INTRODUCTION

Because of their interesting electronic properties and possible application toward future electronic devices, topological materials such as topological insulators, Dirac semimetals, and Weyl semimetals have attracted much attention from physicists, chemists, and materials scientists [1–19]; the basis of topological insulators is reported in Ref. [20]. Among these topological materials, in the past decade topological insulators have been most extensively investigated. A topological insulator is a quantum matter, with a band gap in bulk and gapless states at the surface (or at the edge in two-dimensional cases), which is different from a traditional insulator. The gapless linear dispersion at the surface in a topological insulator is completely protected by time-reversal symmetry, and a pair with linear dispersion (Kramers pair) inevitably emerges. Two linear dispersions which have opposite spins to each other are crossing at $k = 0$, known as the "Dirac point," based on Kramers theorem.

The most studied topological insulator has been Bi_2Se_3, which has a single Dirac cone, i.e., simple surface states [7]. It is well known that the Fermi level of Bi_2Se_3 does not cross the surface states but crosses near a conduction band [10,11,14] as described below. The temperature dependence of resistivity, ρ, shows metallic behavior in Bi_2Se_3 because of a deficiency of Se atoms, providing electrons to tune the Fermi level upward. The Fermi-level tuning to match the Dirac point was achieved by Ca doping, i.e., hole doping by substitution of Bi with Ca, which was confirmed by resistivity, scanning tunneling spectroscopy, and angle-resolved photoelectron spectroscopy (ARPES) measurements [8,12].

Such a Fermi-level tuning was more precisely achieved by adjusting the value of x in $Bi_{2-x}Sb_xTe_{3-y}Se_y$ [13,15]. Namely, the Fermi level decreased with an increase in x, and the Fermi level crossed the Dirac point at $x = 1.0$, which was confirmed by the ARPES [15]. Simultaneously, the Dirac point shifted upward with an increase in x, and increasing x causes a simultaneous increase in y. Therefore, the matching of the Fermi level to the Dirac point is realized at $x = 1.0$ and $y = 2.0$, i.e., $BiSbTeSe_2$. As a result, $Bi_{2-x}Sb_xTe_{3-y}Se_y$ is a suitable material for investigating the correlation between electronic states and physical properties.

Recently, superconductivity in a topological insulator was found in Cu-doped and Sr-doped Bi_2Se_3, providing superconducting transition temperatures, T_c's, as high as 3.8 K for Cu-doped Bi_2Se_3 [21] and 2.2 K for Sr-doped Bi_2Se_3 [22]. The Cu and Sr atoms in the above superconductors are not substituted for Bi, but both atoms are intercalated into the space between two Bi_2Se_3 layers [21,22], which are expressed as "$Cu_xBi_2Se_3$" and "$Sr_xBi_2Se_3$." This implies electron doping for Bi_2Se_3 layers. Surprisingly, the T_c of Sr-doped Bi_2Se_3 ($Sr_{0.065}Bi_2Se_3$) rapidly disappeared with applied pressure, and reemerged with further pressure to reach ~8.3 K at 6 GPa [23]. On the other hand, the substitution of Cu/Sr atom for Bi ($Cu_xBi_{2-x}Se_3$ or $Bi_{1.85}Sr_{0.15}Se_3$) is also possible, but it did not show any superconductivity down to 1.9 K [21,22]. Actually, it is known that nonsuperconducting $Cu_xBi_{2-x}Se_3$ is produced

*kubozono@cc.okayama-u.ac.jp

at $x = 0 - 0.15$, and superconducting $Cu_xBi_2Se_3$ is produced at $x = 0.1-0.15$ [21].

The finding of superconductivity in metal-doped Bi_2Se_3 is exciting from two scientific points of view. First is that the behavior of T_c against pressure means the discovery of pressure-driven T_c enhancement, which suggests a different type of superconducting pairing from that predicted by BCS theory. The second point, which may be more significant, is that the superconductivity may be categorized as "topological superconductivity" characterized by odd parity pairing such as *p*-wave pairing. The temperature dependence of the reduced upper critical field, h^*, fits well with the *p*-wave polar model, suggesting that $Sr_{0.062}Bi_2Se_3$ could be a topological superconductor. Our group also reported pressure-driven superconductivity in Ag-doped Bi_2Se_3, where Ag atom is substituted for Bi, i.e., $Ag_xBi_{2-x}Se_3$ [24]; recent work using both photoelectron and x-ray fluorescence holography suggested the intercalation of Ag in the space between Se layers, as well as substitution. No superconductivity was confirmed in $Ag_{0.05}Bi_{1.95}Se_3$, which is the nominal stoichiometry, at ambient pressure, and superconductivity suddenly appeared at 11 GPa. Two superconducting phases appeared in phase II (space group No. 12, $C2/m$) and phase III (space group No. 139, $I4/mmm$), which transform successively from phase I (space group No. 166, $R\bar{3}m$) with applied pressure. Topological superconductivity was also suggested for $Ag_{0.05}Bi_{1.95}Se_3$ from the temperature dependence of h^*.

Based on the above scientific background, we pursued pressure-driven superconductivity in $Bi_{2-x}Sb_xTe_{3-y}Se_y$ in which the electronic states can be precisely tuned through x and y [15]. Firstly, the crystal structures of $Bi_{2-x}Sb_xTe_{3-y}Se_y$ ($x = 0$, 0.25, 0.5, 1.0, and $y = 1.0$) in a wide pressure range of 0–30 GPa were clarified using powder x-ray diffraction (XRD) with synchrotron radiation. Secondly, the temperature dependence of resistance (R) in the above samples was investigated at 0–15 GPa. Consequently, the successful observation of superconductivity under pressure was achieved for all $Bi_{2-x}Sb_xTe_{3-y}Se_y$ ($x = 0$, 0.25, 0.5, 1.0, and $y = 1.0$) samples. The T_c–pressure (p) phase diagram was drawn for $Bi_{2-x}Sb_xTe_{3-y}Se_y$. Thirdly, the topological nature of pressure-driven superconductivity was investigated from temperature dependence of h^* at high pressure. Finally, the correlation between electronic states and superconductivity was discussed.

II. EXPERIMENTAL

A. Sample preparation and characterization at ambient pressure

Crystals of $Bi_{2-x}Sb_xTe_{3-y}Se_y$ ($x = 0$, 0.25, 0.5, 1.0, and $y = 1.0$) were grown by a conventional melt-growth method using stoichiometric amounts of Bi, Sb, Te, and Se powders, using the following process: the powders were sealed in a quartz tube which was heated at 850 °C for 24 h, then slowly cooled down to 550 °C at a rate of 6 °C/h, and then quenched with ice water. The obtained crystals showed a clear basal plane structure. More details are shown in Supplemental Material, and the XRD patterns of $Bi_{2-x}Sb_xTe_{3-y}Se_y$ ($x = 1.0$, $y = 1.0$) are shown in Fig. S1 to show the high sample quality [25].

The energy-dispersive x-ray (EDX) spectra of the $Bi_{2-x}Sb_xTe_{3-y}Se_y$ samples were recorded with an EDX spectrometer equipped with a scanning electron microscope (KEYENCE VE-9800-EDAX Genesis XM2). The EDX spectra were measured for 5–10 different positions of the $Bi_{2-x}Sb_xTe_{3-y}Se_y$ crystals at room temperature. From the EDX spectra, the chemical compositions of all samples were determined (results are given in Table I).

The crystal structure at ambient pressure was determined by single-crystal XRD measurement of all $Bi_{2-x}Sb_xTe_{3-y}Se_y$ crystals, which were obtained by cutting off a small piece (~100-μm scale) of the crystals, using a Rigaku Saturn 724 diffractometer equipped with a Mo Kα source (wavelength $\lambda = 0.710\,73$ Å); the measurement was performed at 100 K.

B. Measurements of XRD and $R-T$ plot under pressure

Powder XRD patterns of the $Bi_{2-x}Sb_xTe_{3-y}Se_y$ samples were measured under pressure at 297 K, using synchrotron radiation at BL12B2 of SPring-8; the wavelength λ of the x-ray beam was 0.6853 Å. The powder sample obtained by grinding the $Bi_{2-x}Sb_xTe_{3-y}Se_y$ crystal was used for the powder XRD measurement. A diamond-anvil cell (DAC) was used for the high-pressure XRD measurement, with the powder sample loaded into the hole of a stainless-steel plate. Daphne 7373 was used as the pressure medium for XRD measurement under high pressure. The pressure was determined by monitoring ruby fluorescence.

The DC magnetic susceptibility (M/H) of the small crystal (1-mm scale) of $Bi_{2-x}Sb_xTe_{3-y}Se_y$ was recorded by a superconducting quantum interference device (SQUID) magnetometer (Quantum Design MPMS2) at ambient pressure (0 GPa). M and H refer to magnetization and applied magnetic field, respectively. In this SQUID magnetometer, the M/H measurement can be made down to 2.0 K. The temperature dependence of R of $Bi_{2-x}Sb_xTe_{3-y}Se_y$ was measured in four-terminal measurement mode under pressure. The small $Bi_{2-x}Sb_xTe_{3-y}Se_y$ flake was introduced into the DAC in air because this sample is not air sensitive. The sample was loaded directly on a Kapton sheet/epoxy resin/rhenium in the DAC; six Cu electrodes were attached to the Kapton sheet, and this cell was used for measuring the R of the sample. NaCl was used as the pressure medium. The applied pressure was determined by monitoring ruby fluorescence.

The R was measured at 300–1.5 K in standard four-terminal measurement mode using an Oxford superconducting magnet system. The temperature was precisely controlled using an Oxford Instruments MercuryiTC; the minimum temperature is 1.5 K in this equipment. The H was controlled using Oxford Instruments MercuryiPS. Electric current (I) was supplied by a Keithley 220 programmable current source, and the exact value of I was monitored by an Advantest R-8240 digital electrometer. The voltage (V) was measured by an Agilent 34420 digital nanovoltmeter.

III. RESULTS AND DISCUSSION

A. Physical properties of $Bi_{2-x}Sb_xTe_{3-y}Se_y$ at ambient pressure

Optical images of the $Bi_{2-x}Sb_xTe_{3-y}Se_y$ ($x = 0$, 0.25, 0.5, 1.0; $y = 1.0$) crystals are shown in Fig. 1(a). Bright basal

TABLE I. Stoichiometry and structural data of $Bi_{2-x}Sb_xTe_{3-y}Se_y$.

Nominal stoichiometry	Stoichiometry from EDX	Stoichiometry from single-crystal XRD	a (Å)	c (Å)	V (Å^3)	Space group
Bi_2Te_2Se	$Bi_{2.1(1)}Te_{1.8(2)}Se_{1.2(2)}$	$Bi_2Te_{1.46(5)}Se_{1.54(5)}$	4.2609(16)	29.766(16)	468.0(4)	$R\bar{3}m$
$Bi_{1.75}Sb_{0.25}Te_2Se$	$Bi_{1.75(4)}Sb_{0.25(4)}Te_{1.89(7)}Se_{1.11(7)}$	$Bi_{1.68(7)}Sb_{0.31(7)}Te_{1.64(8)}Se_{1.36(8)}$	4.2695(17)	29.869(19)	471.5(4)	$R\bar{3}m$
$Bi_{1.5}Sb_{0.5}Te_2Se$	$Bi_{1.50(3)}Sb_{0.50(3)}Te_{1.68(6)}Se_{1.32(6)}$	$Bi_{1.57(5)}Sb_{0.43(5)}Te_2Se$	4.263(4)	29.99(4)	472.0(9)	$R\bar{3}m$
$BiSbTe_2Se$	$Bi_{1.089(8)}Sb_{0.911(8)}Te_{1.81(3)}Se_{1.19(3)}$	$Bi_{1.1(2)}Sb_{0.9(2)}Te_{1.8(2)}Se_{1.2(2)}$	4.2212(14)	29.869(12)	460.9(3)	$R\bar{3}m$

planes were observed in all crystals. Only peaks ascribable to Bi, Sb, Te, and Se atoms were observed in the EDX spectra, as seen from Fig. 1(b), indicating no contamination by impurities. The averaged stoichiometry determined from the EDX spectrum is listed in Table I. The determined x values are almost consistent with the nominal values in all samples, and the determined y value deviates from the nominal value ($y = 1.0$). The single crystals are homogeneous in stoichiometry, because the estimated standard deviations (esd's) in x and y are small. The lowering of the Fermi level and the raising of the Dirac point against x were confirmed from the ARPES (not shown), in the same manner as those previously reported [15]. As an example, the ARPES of $Bi_{2-x}Sb_xTe_{3-y}Se_y$ ($x = 0.25$) is shown in Fig. S2 in the Supplemental Material [25]; this sample's chemical composition is "$Bi_{1.75(4)}Sb_{0.25(4)}Te_{1.89(7)}Se_{1.11(7)}$" as later described.

The crystal structure determined by single-crystal diffraction at ambient pressure was rhombohedral (space group No. 166: $R\bar{3}m$) for all $Bi_{2-x}Sb_xTe_{3-y}Se_y$, which is consistent with that of Bi_2Se_3 [26] and with that previously determined for Bi_2Te_2Se [27,28]. The lattice constants, a and c, determined are listed in Table I, and the atomic coordinates are listed in Table S1 in Supplemental Material [25]. The lattice constants are close to those of Bi_2Se_3 (4.18 and 28.7 Å) [26]. The values of a and c increase slowly with increasing x, but maximum c value is recorded at $x = 0.5$. Here it is noticed that the y value [$= 1.32(6)$] at $x = 0.5$ determined from EDX is larger than those ($\sim$1.2) at $x = 0$, 0.25, and 1.0. From this result, it may be concluded that the increase in y causes the expansion of the unit cell. The stoichiometry for each $Bi_{2-x}Sb_xTe_{3-y}Se_y$ sample determined from single-crystal XRD is listed in Table I. The stoichiometry determined from single-crystal XRD is almost consistent with that from EDX. Thus, the stoichiometry determined from EDX is reliable. Throughout this paper, the stoichiometry determined from EDX is employed for each $Bi_{2-x}Sb_xTe_{3-y}Se_y$ sample. Crystallographic data of $Bi_{2-x}Sb_xTe_{3-y}Se_y$ samples are listed in Table S1 of Supplemental Material [25].

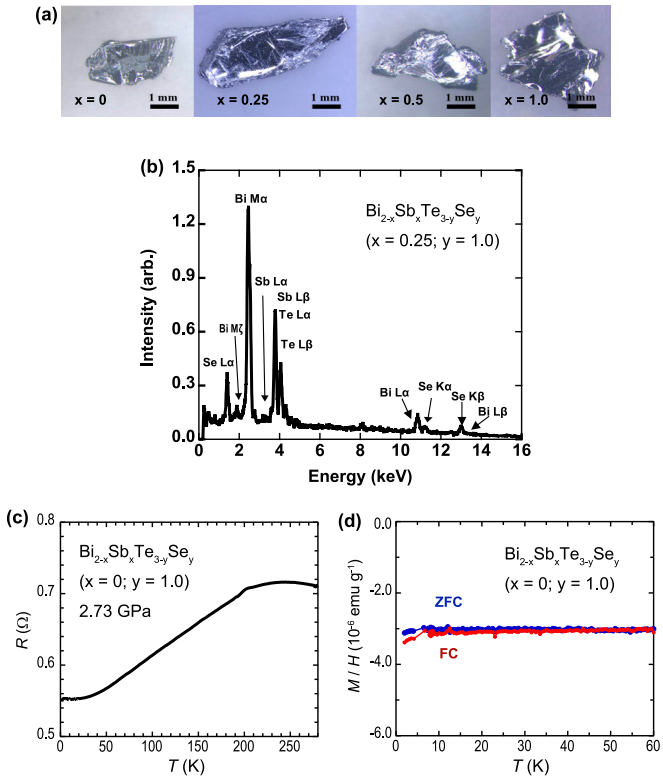

FIG. 1. (a) Optical image and (b) EDX spectrum of a crystal-like lump of $Bi_{2-x}Sb_xTe_{3-y}Se_y$ ($x = 0.25$ and $y = 1.0$). (c) R–T plot and (d) M/H–T plot of $Bi_{2-x}Sb_xTe_{3-y}Se_y$ (nominal $x = 0$ and $y = 1.0$) recorded at 2.73 and 0 GPa, respectively.

Figures 1(c) and 1(d) show temperature dependence of R and magnetic susceptibility (M/H) for $Bi_{2.1(1)}Te_{1.8(2)}Se_{1.2(2)}$ prepared as Bi_2Te_2Se (i.e., nominal x of 0; nominal y of 1.0 for $Bi_{2-x}Sb_xTe_{3-y}Se_y$), respectively, measured at 2.73 GPa and ambient pressure (0 GPa), where M and H refer to magnetization and applied magnetic field, respectively. No superconductivity is observed near ambient pressure, as seen from Figs. 1(c) and 1(d). The R–T plot [Fig. 1(c)] at 2.73 GPa substantially shows metallic behavior. Strictly speaking, the R saturates at higher temperature than 200 K. This behavior may be due to the fact that the Fermi level does not match the bulk conduction band, but crosses the bottom of the conduction band or the top of surface states [15]. The M/H–T plots for other $Bi_{2-x}Sb_xTe_{3-y}Se_y$ samples (i.e., nominal $x = 0.25$, 0.5 and 1.0; nominal $y = 1.0$) did not show any superconducting transition at low pressure (not shown). Thus, all $Bi_{2-x}Sb_xTe_{3-y}Se_y$ samples are not superconductors at ambient pressure.

B. Pressure dependence of crystal structure of $Bi_{2-x}Sb_xTe_{3-y}Se_y$

Figures 2(a)–2(d) show XRD patterns of $Bi_{2-x}Sb_xTe_{3-y}Se_y$ samples under pressure up to 29 GPa. As seen from Fig. 2(a), the XRD patterns of $Bi_{2.1(1)}Te_{1.8(2)}Se_{1.2(2)}$ at 2.4–29 GPa show the presence of three different phases (phase I, phase II, and phase III) which were assigned to rhombohedral (space group No. 166, $R\bar{3}m$), monoclinic (space group No. 12, $C2/m$), and 9/10-fold monoclinic (space group No. 12, $C2/m$), respectively. These crystal structures are shown in

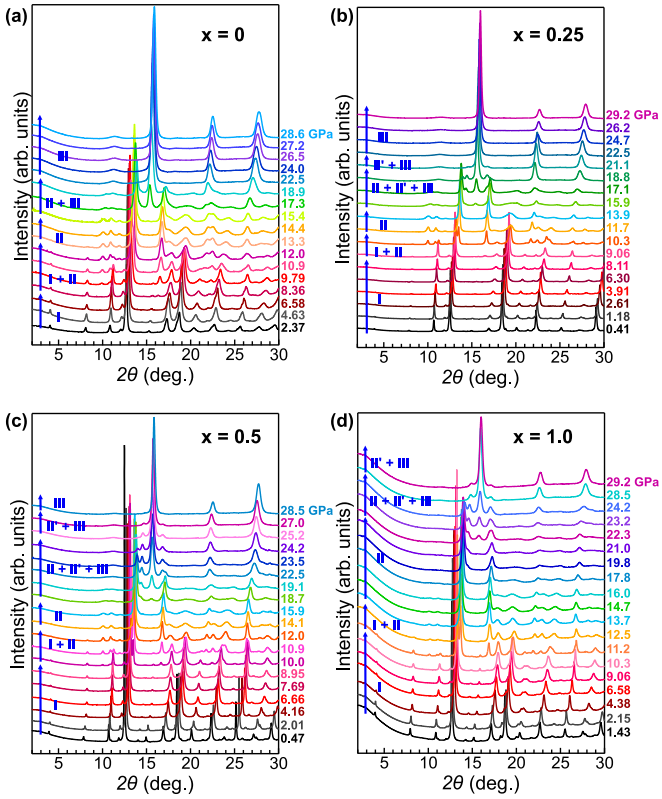

FIG. 2. Pressure-dependent powder XRD patterns of $Bi_{2-x}Sb_xTe_{3-y}Se_y$ with nominal x values of (a) 0, (b) 0.25, (c) 0.5, and (d) 1.0; nominal y value is 1.0 for all samples. Measurement temperature and pressure are 297 K and 0–30 GPa, respectively.

Fig. 3. The crystal structures of phase I and phase II are the same as those previously determined [27,28]. However, the crystal structure of phase III is different from those reported in Refs. [27] and [28], and was the same as that for Bi_2Te_3 and Bi_2Se_3 reported in Refs. [29] and [30]. In this study, we performed Le Bail fitting for the XRD pattern based

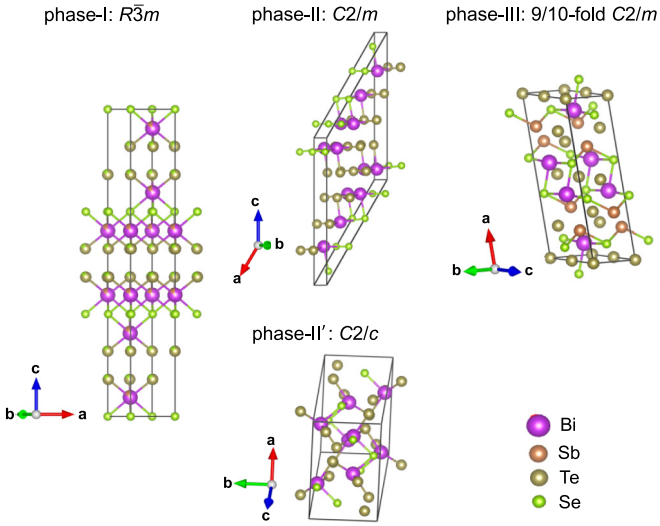

FIG. 3. Crystal structures of phase I, phase II, phase II', and phase III in $Bi_{2-x}Sb_xTe_{3-y}Se_y$.

on various space groups suggested for Bi_2Te_3 [29,31,32], Bi_2Se_3 [30,33–37], Sb_2Se_3 [38,39], and Sb_2Te_3 [40–43], and $Bi_{2-x}Sb_xTe_{3-y}Se_y$ [27,28,44,45], and the experimental XRD pattern of $Bi_{2.1(1)}Te_{1.8(2)}Se_{1.2(2)}$ for each phase was most exactly fitted by the above space group: rhombohedral structure (space group No. 166, $R\bar{3}m$) for phase I, monoclinic structure (space group No. 12, $C2/m$) for phase II, and 9/10-fold monoclinic structure (space group No. 12, $C2/m$) for phase III).

For showing the quality of fit between experimental and calculated XRD pattern in $Bi_{2-x}Sb_xTe_{3-y}Se_y$, the experimental XRD patterns of $Bi_{2.1(1)}Te_{1.8(2)}Se_{1.2(2)}$ at 2.37, 14.4, and 28.6 GPa are shown in Fig. S3 [25], with the patterns calculated by Le Bail fitting. All XRD peaks are well fitted, as seen from Fig. S3 [25]. The values of weighted pattern R factor (wR_p), pattern R factor (R_p), and χ^2 in the Le Bail fitting were 2.98%, 1.48%, and 0.921 for 2.37 GPa; 2.13%, 1.15%, and 0.743 for 14.4 GPa; and 1.60%, 0.96%, and 0.449 for 28.6 GPa. The values of wR_p and R_p in the Le Bail fitting for pressure-dependent XRD patterns were less than 3% for $Bi_{2.1(1)}Te_{1.8(2)}Se_{1.2(2)}$, less than 4% for $Bi_{1.75(4)}Sb_{0.25(4)}Te_{1.89(7)}Se_{1.11(7)}$, less than 7.0% for $Bi_{1.50(3)}Sb_{0.50(3)}Te_{1.68(6)}Se_{1.32(6)}$, and less than 4.5% for $Bi_{1.089(8)}Sb_{0.911(8)}Te_{1.81(3)}Se_{1.19(3)}$, indicating the good fit between the experimental and calculated XRD patterns.

In this study, we partly performed Rietveld refinement for XRD patterns at 2.37 GPa (phase I), 14.4 GPa (phase II), and 28.6 GPa (phase III) for $Bi_{2.1(1)}Te_{1.8(2)}Se_{1.2(2)}$ to obtain the atomic coordinates. All XRD patterns are well refined based on the above space group (space group No. 166, $R\bar{3}m$ for phase I, space group No. 12, $C2/m$ for phase II, and space group No. 12, $C2/m$ for phase III), as seen from Fig. S4 [25], indicating the validity of the space group suggested for each phase; the values of wR_p, R_p, and χ^2 in the Rietveld analyses were 3.21%, 1.83%, and 1.06, for 2.37 GPa; 2.40%, 1.81%, and 0.938 for 14.4 GPa; and 1.36%, 1.00%, and 0.320 for 28.6 GPa. The lattice constants determined by Rietveld refinement are the same as those determined by Le Bail fitting. The lattice constants and atomic coordinates determined in the Rietveld analyses are listed in Table S2 [25].

The first and second structural phase transitions are observed at 8.36 and 15.4 GPa, respectively, for $Bi_{2.1(1)}Te_{1.8(2)}Se_{1.2(2)}$. Actually, it is noticed that multiple phases exist around the above pressures. Namely, phase I still remains even above 8.36 GPa, although phase II emerges at 8.36 GPa. Only phase II is found from 13.3 GPa. Such a coexistence of multiple phases (phase II and phase III) is observed at 15.4–18.9 GPa, and a single phase (phase III) exists from 22.5 GPa. As a consequence, the structural transition is not sharp but broad, i.e., pressure width of a few GPa is observed for the complete structural transition. For a simple understanding of the evolution of structure against pressure, a schematic representation is given in Fig. 4(a). In addition, our results on crystal structures for phase I and phase II are consistent with those reported previously for Bi_2Te_2Se [27,28,45], and the crystal structure for phase III is different from those (space group No.229, $Im\bar{3}m$ [27], space group No.139, $I4/mmm$ [28,45]) reported previously. However, our suggested structure (space group No. 12, $C2/m$) provided the better fit between the experimental and calculated XRD patterns both in Le Bail fitting and Rietveld refinement.

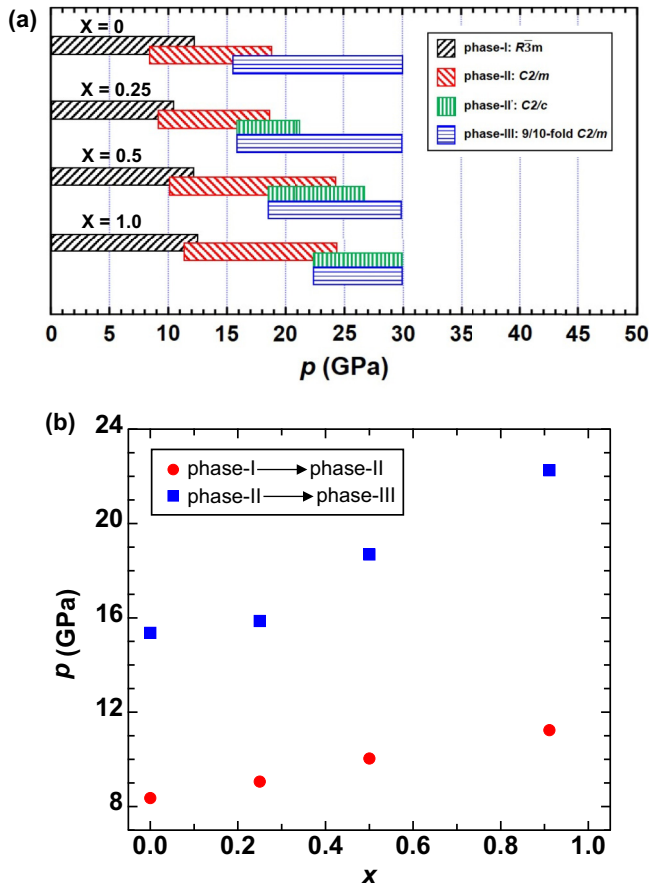

FIG. 4. (a) Schematic representation of evolution of crystal structure against pressure, and (b) x dependence of pressure causing structural transitions (phase I to phase II, and phase II to phase III) in $Bi_{2-x}Sb_xTe_{3-y}Se_y$.

In addition, the monoclinic structure (space group No. 12, $C2/m$) corresponds to the distorted structure of the above body-centered cubic structure (space group No.229, $Im\bar{3}m$), or body-centered tetragonal structure (space group No.139, $I4/mmm$).

As seen from the XRD patterns shown in Figs. 2(b)–2(d), $Bi_{1.75(4)}Sb_{0.25(4)}Te_{1.89(7)}Se_{1.11(7)}$, $Bi_{1.50(3)}Sb_{0.50(3)}Te_{1.68(6)}Se_{1.32(6)}$, and $Bi_{1.089(8)}Sb_{0.911(8)}Te_{1.81(3)}Se_{1.19(3)}$ have four different phases (phase I, phase II, phase II', and phase III) for each sample under pressure up to 30 GPa; the nominal x and y values for the above samples are listed in Table I. Here, it should be noticed that phase II' is additionally observed although only three phases are found in $Bi_{2.1(1)}Te_{1.8(2)}Se_{1.2(2)}$ [Fig. 2(a)]. The crystal structures of main phases, phase I, phase II, and phase III, are the same as those in $Bi_{2.1(1)}Te_{1.8(2)}Se_{1.2(2)}$. The crystal structure of phase II' was assigned to monoclinic structure (space group No. 15, $C2/c$). The atomic coordinates and lattice constants in the monoclinic structures of phase II, phase II', and phase III are different from each other [28], and as described later, the discontinuous change of lattice constants and volume is observed between monoclinic phases. The pressures for transitions of phase I to phase II and phase II to phase III were 9.06 and 15.9 GPa for $Bi_{1.75(4)}Sb_{0.25(4)}Te_{1.89(7)}Se_{1.11(7)}$, respectively. The pressures were 10.0 and 18.7 GPa for $Bi_{1.50(3)}Sb_{0.50(3)}Te_{1.68(6)}Se_{1.32(6)}$, and 11.2 and 22.3 GPa for $Bi_{1.089(8)}Sb_{0.911(8)}Te_{1.81(3)}Se_{1.19(3)}$; the crystal phases determined for phase I and phase II are the same as those reported previously for $Bi_{1.5}Sb_{0.5}Te_{1.8}Se_{1.2}$ [$Bi_{2-x}Sb_xTe_{3-y}Se_y$ ($x = 0.5$)] [45], indicating the reliability of our crystal data. However, our suggested crystal structure for phase III (space group No. 12, $C2/m$) is different from that reported previously (space group No.139, $I4/mmm$ [45]). Our suggested crystal structure provided the better fit between experimental and calculated XRD patterns as in Bi_2Te_2Se. No crystal data under pressure have been reported for $Bi_{2-x}Sb_xTe_{3-y}Se_y$ ($x = 0.25$ and 1.0).

In the same manner as $Bi_{2.1(1)}Te_{1.8(2)}Se_{1.2(2)}$, multiple phases exist around the above pressures, as seen from Figs. 2(b)–2(d) and Fig. 4(a). Figure 4(b) shows the pressures causing structural phase transitions (phase I to phase II and phase II to phase III) for each sample. Both pressures for phase I to phase II and phase II to phase III monotonically increase with an increase in x, i.e., amount of Sb. Actually, as seen from Figs. 2(b)–2(d), phases II' emerges together with phase II and/or phase III in the $Bi_{2-x}Sb_xTe_{3-y}Se_y$ samples other than $Bi_{2.1(1)}Te_{1.8(2)}Se_{1.2(2)}$, and still exists even in phase III; the schematic representation of phases against pressure is shown in Fig. 4(a).

The lattice constants (a and c) against pressure for the $Bi_{2-x}Sb_xTe_{3-y}Se_y$ samples are shown in Figs. S5(a)–S5(d) [25]. The discontinuous change of lattice constants is observed with each structural transition, indicating the first-order transition. The V/Z value monotonously decreases with an increase in pressure (Fig. 5), and discontinuous changes (sudden drop) are observed at the pressures corresponding to structural transitions [Figs. 5(a)–5(d)]; the Z is the number of asymmetry units in each crystal lattice, and V/Z corresponds to the volume per a $Bi_{2-x}Sb_xTe_{3-y}Se_y$. As seen from Figs. 5(a)–5(d), two or three phases coexist at a part of the region in phase II and phase III. Moreover, the ratios of lattice constants at each pressure with respect to that at minimum pressure in each phase (phase I, phase II, and phase III) of $Bi_{2-x}Sb_xTe_2Se$ ($x = 0.25$) are illustrated in Figs. S6–S8, indicating an extremely small anisotropy for contraction against pressure in all phases. Admittedly, the c/c(0.41 GPa) is slightly smaller than a/a(0.41 GPa) in phase I, but the difference is within 2% (Fig. S6). In other phases, the difference at each lattice constant is within ~4% (see Figs. S7 and S8). Thus, the anisotropy of contraction in all phases is negligible.

Finally, we must comment on the peak broadening in pressure-dependent XRD which would be caused by use of Daphne 7373 as pressure medium. Admittedly, the Daphne 7373 may be generally available as pressure medium for keeping the static pressure up to 10 GPa, and above 10 GPa the peak broadening may take place. Nevertheless, the lattice constants and V were definitely determined with very small esd's up to 30 GPa, indicating the structural parameters obtained are reliable.

C. Pressure dependence of physical properties of $Bi_{2-x}Sb_xTe_{3-y}Se_y$

Figure 6(a) shows the temperature dependence of R in $Bi_{2.1(1)}Te_{1.82(2)}Se_{1.1(2)}$ at different pressures, where

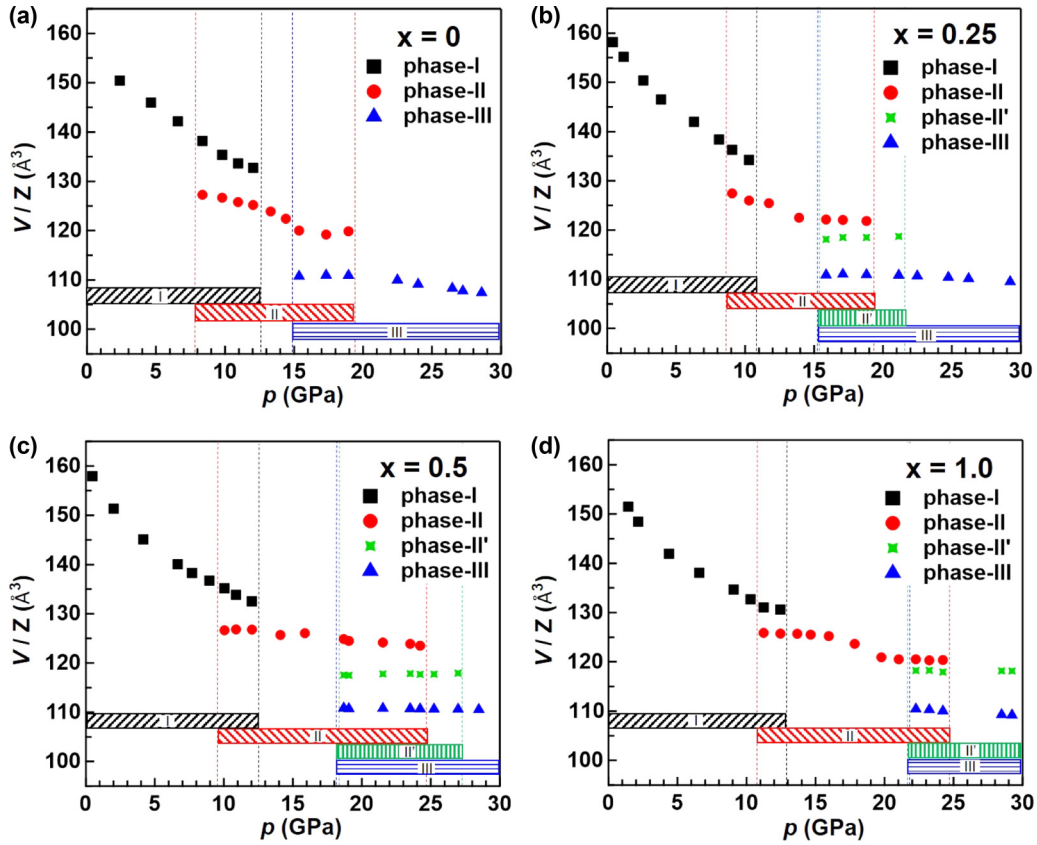

FIG. 5. Pressure dependence of V of $Bi_{2-x}Sb_xTe_{3-y}Se_y$ (V/Z) with nominal x values of (a) 0, (b) 0.25, (c) 0.5, and (d) 1.0; nominal y value is 1.0 for all samples. Chemical composition for each sample is listed in Table I. Z is the number of asymmetry unit.

$R/R(10\ K)$ is plotted, i.e., the R is normalized at 10 K so that all data obtained in the different measurements can be reasonably compared. The $R/R(10\ K)$–T plots at 0–2 GPa show no superconductivity down to 1.5 K in increasing pressure, while a clear superconducting transition appears above 2.5 GPa which is in phase I. Figure 6(b) shows the T_c-p plot in $Bi_{2.1(1)}Te_{1.8(2)}Se_{1.2(2)}$, in which the T_c values are determined from the $R/R(10\ K)$–T plots at different pressures shown in Fig. 6(a). As seen from Fig. 6(b), the T_c monotonically increases with an increase in pressure. No significant variation in T_c-p plot is observed at the structural transition of phase I to phase II. Here, we comment that a complete disappearance of R drop for all $Bi_{2-x}Sb_xTe_{3-y}Se_y$ samples is clearly confirmed under H as high as several tesla. These results indicate that the R drop originates from the superconducting transition. Examples of H dependence of $R/R(10\ K)$–T plots under pressure are shown in Figs. 7(a) and 7(c), as described later. We must briefly comment on nonvanishing R at the superconducting state in the $R/R(10\ K)$–T plots (Figs. 6 and 7). As seen from Figs. 6(a), 7(a), and 7(c), the complete zero resistance (zero-R) even in the superconducting state is not observed because of polycrystallinity of the sample employed in resistance measurement under pressure, i.e., the resistance at grain boundaries between single crystals provides nonvanishing R in the superconducting state.

Figure 6(b) shows the T_c-p plots in the other $Bi_{2-x}Sb_xTe_{3-y}Se_y$ samples ($Bi_{1.75(4)}Sb_{0.25(4)}Te_{1.89(7)}Se_{1.11(7)}$, $Bi_{1.50(3)}Sb_{0.50(3)}Te_{1.68(6)}Se_{1.32(6)}$, and $Bi_{1.089(8)}Sb_{0.911(8)}Te_{1.81(3)}Se_{1.19(3)}$). The T_c value was determined from the cross point between R drop and R–T plot in the normal state, as seen from Fig. S9(a) in Supplemental Material [25]. All samples show no superconductivity at low pressures below 3 GPa, and the superconductivity emerged in phase I. The T_c increases with an increase in pressure, and any discontinuous variation is not observed at structural phase transition (phase I to phase II), as seen from Fig. 6(b). Actually, the T_c for $Bi_{1.50(3)}Sb_{0.50(3)}Te_{1.68(6)}Se_{1.32(6)}$ rapidly and continuously increases at 10 GPa, at which the phase II appears. When decreasing pressure, the superconductivity of the above samples could be kept down to lower pressure than the pressure at which the superconductivity emerges in increasing pressure (or onset pressure), indicating the presence of hysteresis in the T_c-p plot. The behavior of T_c against pressure is similar in all $Bi_{2-x}Sb_xTe_{3-y}Se_y$ samples, inclusive of $Bi_{2.1(1)}Te_{1.82(2)}Se_{1.1(2)}$. The pressure at which the superconductivity emerges and the maximum T_c for all $Bi_{2-x}Sb_xTe_{3-y}Se_y$ samples are listed in Table II; the maximum T_c of 5.45 K is recorded at 13.5 GPa for $Bi_{2.1(1)}Te_{1.82(2)}Se_{1.1(2)}$ in the pressure range of 0–15 GPa. The T_c values for all samples still increase in the pressure range achieved in this study, and each T_c continuously varies at phase I and phase II, indicating that the density of states (DOS) on the Fermi level may increase with a shrinkage of lattice volume, although the behavior cannot simply be explained. To clarify the mechanism of the increase in T_c against pressure more, a theoretical evaluation of electronic

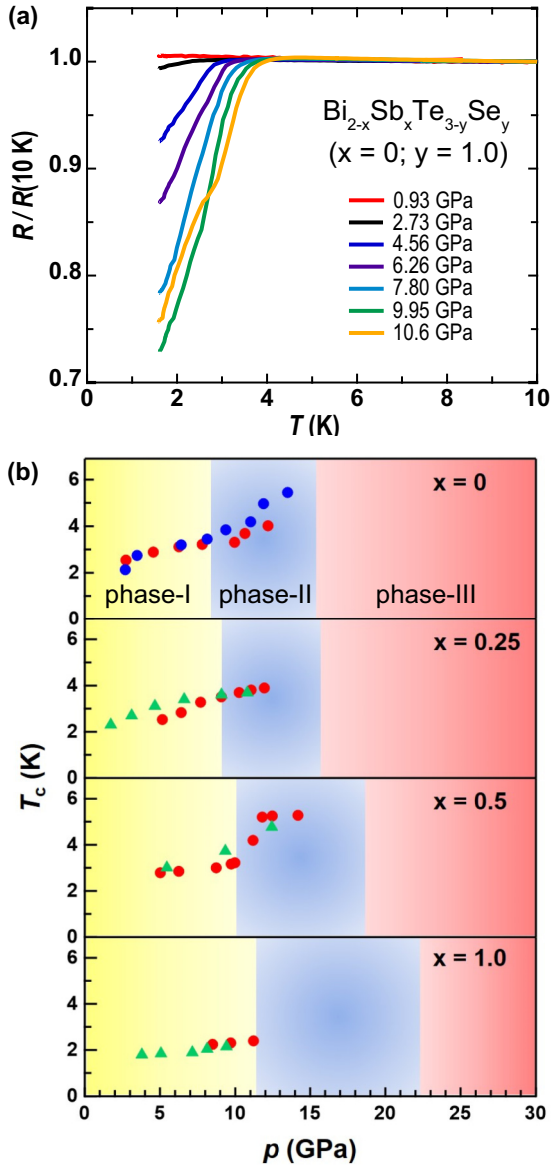

FIG. 6. (a) $R/R(10\ \mathrm{K})$–T plots at different pressures for $Bi_{2-x}Sb_xTe_{3-y}Se_y$ with nominal x value of 0 and nominal y of 1.0. Chemical composition is "$Bi_{2.1(1)}Te_{1.8(2)}Se_{1.2(2)}$, " which is determined from EDX. (b) T_c-p plots for $Bi_{2-x}Sb_xTe_{3-y}Se_y$ with nominal x value of 0, 0.25, 0.5m and 1.0; nominal y is 1.0. Chemical compositions for the above samples determined from EDX are listed in Table I. Red and blue circles for $x = 0$ refer to the first and second measurements, which were recorded in increasing pressure. Red circle and green triangle for $x = 0.25$, $x = 0.5$, and $x = 1.0$ refer to plots recorded in increasing and decreasing pressure.

states of $Bi_{2-x}Sb_xTe_{3-y}Se_y$ under pressure was performed for three selected structures, indicating the enhancement of DOS with increasing pressure (Figs. S10–S12 [25]). Namely, the increase in T_c against pressure may be due to the DOS enhancement. In addition, the Hall-effect measurement under pressure may be efficient to experimentally confirm the change of carrier density and DOS, which may be a future task.

Here, we must consider why superconductivity for $Bi_{2-x}Sb_xTe_{3-y}Se_y$ emerged in phase I, different from Bi_2Se_3 and Ag-doped Bi_2Se_3 in which superconductivity appeared in phase II [24,37]. This result seems to be quite strange. However, it should be noticed that pressure-induced superconductivity was observed in phase I for Bi_2Te_3 [46]. Namely, the observation of superconductivity in phase I may not be unusual for mixed compounds of Se and Te such as $Bi_{2-x}Sb_xTe_{3-y}Se_y$. In other words, the behavior of superconductivity against pressure well reflects the feature of Bi_2Te_3. This could explain that the above difference is a reasonable phenomenon, although this may not be a complete explanation.

In this study, we did not apply more pressure to the samples because of experimental problems; the pressure could not be increased to a pressure above 15 GPa because of the small culet size of diamond used in this study. To solve this problem, it is necessary to make a small hole in the gasket, and this is now in progress. As a result, the behavior of T_c at phase III could not be characterized in the present study, and it is a future task.

D. Magnetic-field dependence of $R-T$ plot of $Bi_{2-x}Sb_xTe_{3-y}Se_y$ under pressure

The $R/R(10\ \mathrm{K})$–T plots of $Bi_{1.75(4)}Sb_{0.25(4)}Te_{1.89(7)}Se_{1.11(7)}$ under magnetic field (H) at 7.69 GPa is shown in Fig. 7(a). This pressure corresponds to phase I. The R drop is suppressed with an increase in H up to 2.0 T, and the T_c decreases; we evaluated the T_c value which is defined as the temperature providing 99% of the maximum R in the temperature range between the superconducting and normal states, as shown in Fig. S9(b) [25]. The values of the reduced critical field, $h^*(T) = [\frac{H_{c2}(T)}{T_c}]/[-\frac{dH_{c2}(T)}{dT}]_{T=T_c} = \frac{H_{c2}(T)}{T_c \times [-\frac{dH_{c2}(T)}{dT}]_{T=T_c}} = \frac{H_{c2}(T)}{H_{c2}(0)}$, of $Bi_{1.75(4)}Sb_{0.25(4)}Te_{1.89(7)}Se_{1.11(7)}$ at 7.69 GPa were plotted as a function of t $(= \frac{T}{T_c})$, as shown in Fig. 7(b); the $h^*(t)-t$ plot was prepared based on the $H_{c2}-T_c$ plot evaluated from the R–T plots shown in Fig. 7(a); the error bar in Fig. 7(b) is within the symbol (red circle) because the T_c is determined by the above way.

The $h^*(t)-t$ plot was fitted using three different models [47–50], Werthamer-Helfand-Hohenberg (WHH) theory,

TABLE II. Pressure dependence of superconductivity in $Bi_{2-x}Sb_xTe_{3-y}Se_y$.

Nominal stoichiometry	Stoichiometry from EDX	Onset pressure for superconductivity (GPa)	Maximum T_c (K)	Pressure showing maximum T_c (GPa)
Bi_2Te_2Se	$Bi_{2.1(1)}Te_{1.8(2)}Se_{1.2(2)}$	2.69	5.45	13.5
$Bi_{1.75}Sb_{0.25}Te_2Se$	$Bi_{1.75(4)}Sb_{0.25(4)}Te_{1.89(7)}Se_{1.11(7)}$	5.15	3.90	11.9
$Bi_{1.5}Sb_{0.5}Te_2Se$	$Bi_{1.50(3)}Sb_{0.50(3)}Te_{1.68(6)}Se_{1.32(6)}$	5.02	5.28	14.2
$BiSbTe_2Se$	$Bi_{1.089(8)}Sb_{0.911(8)}Te_{1.81(3)}Se_{1.19(3)}$	8.49	2.40	11.2

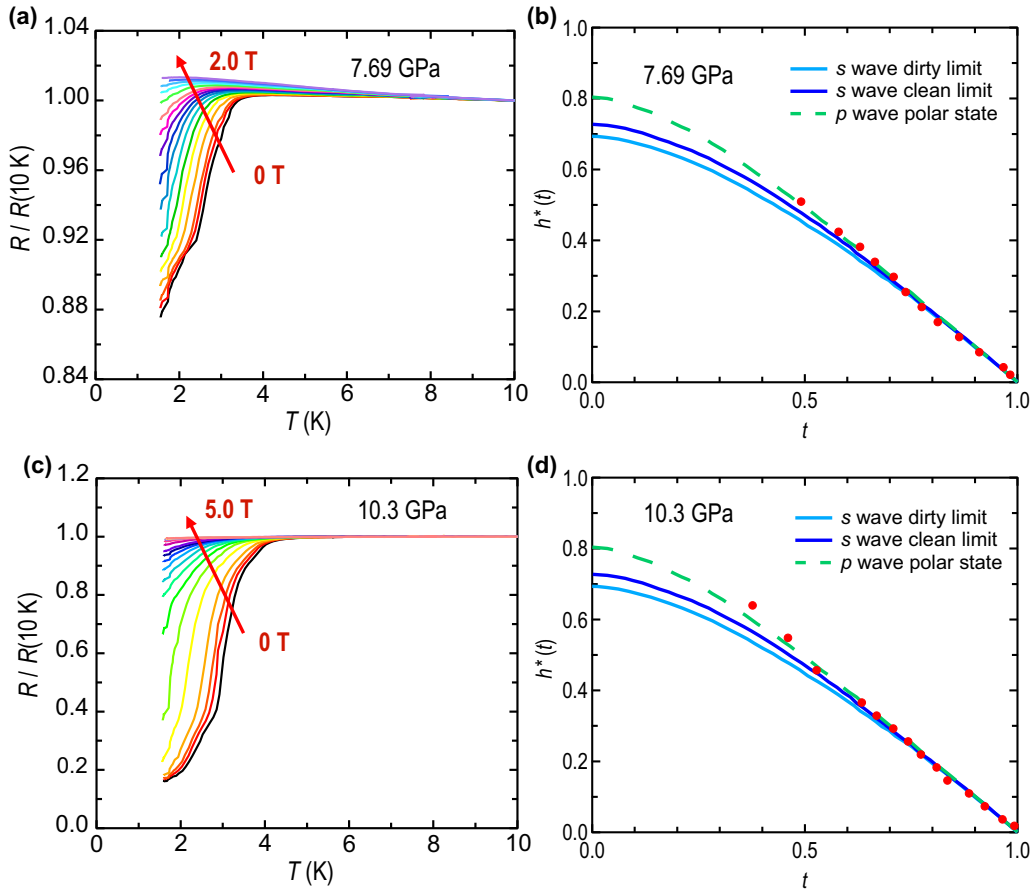

FIG. 7. $R/R(10\ \mathrm{K})$–T plots for $Bi_{2-x}Sb_xTe_{3-y}Se_y$ ($x = 0.25$, $y = 1.0$) under magnetic field H at (a) 7.69 GPa and (c) 10.3 GPa. $h^* - t$ plots for $Bi_{2-x}Sb_xTe_{3-y}Se_y$ ($x = 0.25$, $y = 1.0$) at (b) 7.69 GPa and (d) 10.3 GPa. Chemical composition of the sample is "$Bi_{1.75(4)}Sb_{0.25(4)}Te_{1.89(7)}Se_{1.11(7)}$, " which is determined from EDX. A very small kink observed at around 2.0 K in (a) and (c) is due to the problem of equipment, which never affects the T_c determination necessary for drawing the graphs in (b) and (d).

which corresponds to the *s*-wave dirty-limit superconductivity, *s*-wave clean-limit model, and *p*-wave polar model. The WHH theory predicts $h^*(0) = 0.69$ at $t = 0$, but the experimental $h^*(0)$ does not converge to the value, which is the same as that of $Sr_{0.065}Bi_2Se_3$ [23] and $Ag_{0.05}Bi_{1.95}Se_3$ [24]. The $h^*(0)$ value should become 0.80–0.85 for the *p*-wave polar model [23,33,48,50]. The experimental $h^*(t) - t$ plot seems to be well followed by the *p*-wave model [see Fig. 7(b)], rather than the theoretical curve of *s*-wave clean/dirty limit. However, the data points are insufficient to conclude the topological superconductivity. Therefore, we have not concluded the *p*-wave pairing for the superconductivity for $Bi_{1.75(4)}Sb_{0.25(4)}Te_{1.89(7)}Se_{1.11(7)}$ at 7.69 GPa, but it must be fully pursued in the future work. In addition, the experimental results that the superconducting transition is broadened and R does not go to zero [Figs. 7(a) and 7(c)] with increasing H under pressure may be due to the chemical and electronic inhomogeneity, fluctuation, and vortex effects, in addition to finite resistance at grain boundaries.

The $R/R(10\ \mathrm{K})$–T plot of $Bi_{1.75(4)}Sb_{0.25(4)}Te_{1.89(7)}Se_{1.11(7)}$ at 10.3 GPa is shown in Fig. 7(c), and the R drop is suppressed with an increase in H up to 5.0 T. This pressure corresponds to phase II. The h^*-t plot is shown in Fig. 7(d); the error bar is also within the symbol (red circle). The plot is also fitted by the *p*-wave polar model, indicating a possible topological superconductivity. In summary, the possibility that pressure-induced superconducting phase of $Bi_{1.75(4)}Sb_{0.25(4)}Te_{1.89(7)}Se_{1.11(7)}$ is an unconventional superconductor (or topological superconductor) must be fully investigated as a future task. In addition, the pressure-induced superconducting phase seems to have the same nature between phase I and phase II, showing that the superconductivity may not be correlated with structural transition. Furthermore, in Supplemental Material [25], the topological nature in superconductivity is briefly discussed based on the $h^* - t$ plots of other $Bi_{2-x}Sb_xTe_{3-y}Se_y$ samples under pressure, indicating that the possibility of *p*-wave pairing must be pursued in the pressure-induced superconducting phases.

Moreover, the exploratory density-functional theory calculations for $Bi_{2-x}Sb_xTe_{3-y}Se_y$ ($x = 0$ and $y = 1.0$), Bi_2Te_2Se, were performed to investigate topological nature in each phase under pressure. The detailed information is described in Supplemental Material [25] (see also Refs. [51,52] therein). From the Z_2 invariants for phase I, phase II, and phase III, the topological superconductivity (*p*-wave pairing) suggested from h^*-t plots may be reasonable for phase I. This result must also be ascertained in detail.

In addition, we evaluated the Ginzburg-Landau (GL) coherence length (ξ_{GL}) using expression, $H'_{c2}(0) = \frac{\Phi_0}{2\pi\xi^2_{\mathrm{GL}}}$, from the upper critical magnetic field, $H'_{c2}(0)$

$(= 0.80[\frac{\partial H_{c2}}{\partial T}]_{T=T_c})$, determined based on p-wave polar model to be 132 Å for 7.96 GPa and 87 Å for 10.3 GPa in $Bi_{1.75(4)}Sb_{0.25(4)}Te_{1.89(7)}Se_{1.11(7)}$; Φ_0 is 2.0678×10^{-7} G cm^2. Thus, the ξ_{GL} value somewhat decreased with increasing pressure, indicating the existence of chemical inhomogeneity and granular effect at high pressure.

IV. CONCLUSION AND REMARKS

In this study, the pressure dependence of crystal structure and physical properties are fully investigated, and three or four phases were found in $Bi_{2-x}Sb_xTe_{3-y}Se_y$. No superconductivity for all $Bi_{2-x}Sb_xTe_{3-y}Se_y$ samples with nominal x of 0, 0.25, 0.5, and 1.0, as well as nominal $y = 1.0$, was observed at ambient pressure. Superconductivity appeared in phase I by applying pressure to these samples. The T_c gradually increased with an increase in pressure, and it continuously varied from phase I to phase II. No other superconducting phases appeared. The h^*-t plots recorded in both phases of I and II for $Bi_{1.75(4)}Sb_{0.25(4)}Te_{1.89(7)}Se_{1.11(7)}$ and $Bi_{1.50(3)}Sb_{0.50(3)}Te_{1.68(6)}Se_{1.32(6)}$ were well fitted by the p-wave polar model, indicating the topological nature of superconductivity, or at least the necessity of pursuit of topological superconductivity.

The most important point in this study is whether superconductivity changes against the variation of electronic states where the Fermi level decreases and the Dirac point increases with an increase in x. The pressures causing the structural transitions from phase I to phase II, and from phase II to phase III, systematically increased with an increase in x, while the behavior of T_c against pressure was almost similar among all samples, i.e., the T_c values for all samples continuously increased with an increase in pressure. On the other hand, the insulating behavior in the normal state at low pressure (below 3 GPa) was substantially observed for $Bi_{2-x}Sb_xTe_{3-y}Se_y$ with $x \neq 0$, while clear metallic behavior was observed for $x = 0$. This result may be reasonably understood when considering the energy difference between the Fermi level and the bulk conduction/valence bands. Through this study, we achieved a systematic study of pressure-driven superconductivity in $Bi_{2-x}Sb_xTe_{3-y}Se_y$. In particular, the findings of the appearance of superconductivity from phase I, the continuous increase in T_c against structural change of phase I to phase II, and the suggested topological nature in superconductivity would be a first step not only for the discovery of the pressure-driven high-T_c phase in topological materials but also for pioneering topological superconductor.

ACKNOWLEDGMENT

The authors appreciate Yanan Wang, Huan Li, and Lei Zhi for their kind cooperation with the transport experiments under pressure. This study was partly supported by JSPS KAKENHI Grants No. 26105004, No. 15K21732, No. 17K05500, No. 18K03540, No. 18K04940, No. 18K18736, and No. 19H02676. The XRD measurements at SPring-8 were carried out under Proposals No. 2017B1336, No. 2017B4133, No. 2018A4132, and No. 2018B4140.

[1] C. L. Kane and E. J. Mele, Z_2 Topological Order and the Quantum Spin Hall Effect, Phys. Rev. Lett. **95**, 146802 (2005).

[2] J. E. Moore and L. Balents, Topological invariants of time-reversal-invariant band structures, Phys. Rev. B **75**, 121306(R) (2007).

[3] L. Fu and C. L. Kane, Topological insulators with inversion symmetry, Phys. Rev. B **76**, 045302 (2007).

[4] D. Hsieh, D. Qian, L. Wray, Y. Xia, Y. S. Hor, R. J. Cava, and M. Z. Hasan, A topological Dirac insulator in a quantum spin Hall phase, Nature (London) **452**, 970 (2008).

[5] Y. L. Chen, J. G. Analytis, J. H. Chu, Z. K. Liu, S. K. Mo, X. L. Qi, H. J. Zhang, D. H. Lu, X. Dai, Z. Fang, S. C. Zhang, I. R. Fisher, Z. Hussain, and Z. X. Shen, Experimental realization of a three-dimensional topological insulator, Bi_2Te_3, Science **325**, 178 (2009).

[6] D. Hsieh, Y. Xia, D. Qian, L. Wray, F. Meier, J. H. Dil, J. Osterwalder, L. Patthey, A. V. Fedorov, H. Lin, A. Bansil, D. Grauer, Y. S. Hor, R. J. Cava, and M. Z. Hasan, Observation of Time-Reversal-Protected Single-Dirac-Cone Topological-Insulator States in Bi_2Te_3 and Sb_2Te_3, Phys. Rev. Lett. **103**, 146401 (2009).

[7] Y. Xia, D. Qian, D. Hsieh, L. Wray, A. Pal, H. Lin, A. Bansil, D. Grauer, Y. S. Hor, R. J. Cava, and M. Z. Hasan, Observation of a large-gap topological-insulator class with a single Dirac cone on the surface, Nat. Phys. **5**, 398 (2009).

[8] Y. S. Hor, A. Richardella, P. Roushan, Y. Xia, J. G. Checkelsky, A. Yazdani, M. Z. Hasan, N. P. Ong, and R. J. Cava, p-type Bi_2Se_3 for topological insulator and low-temperature thermoelectric applications, Phys. Rev. B **79**, 195208 (2009).

[9] H. J. Zhang, C. X. Liu, X. L. Qi, X. Dai, Z. Fang, and S. C. Zhang, Topological insulators in Bi_2Se_3, Bi_2Te_3 and Sb_2Te_3 with a single Dirac cone on the surface, Nat. Phys. **5**, 438 (2009).

[10] J. G. Analytis, J. H. Chu, Y. L. Chen, F. Corredor, R. D. McDonald, Z. X. Shen, and I. R. Fisher, Bulk Fermi surface coexistence with Dirac surface state in Bi_2Se_3: A comparison of photoemission and Shubnikov-de Haas measurements, Phys. Rev. B **81**, 205407 (2010).

[11] D. O. Scanlon, P. D. C. King, R. P. Singh, A. de la Torre, S. M. Walker, G. Balakrishnan, F. Baumberger, and C. R. A. Catlow, Controlling bulk conductivity in topological insulators: Key role of anti-site defects, Adv. Mater. **24**, 2154 (2012).

[12] Z. Y. Wang, T. Lin, P. Wei, X. F. Liu, R. Dumas, K. Liu, and J. Shi, Tuning carrier type and density in Bi_2Se_3 by Ca-doping, Appl. Phys. Lett. **97**, 042112 (2010).

[13] Z. Ren, A. A. Taskin, S. Sasaki, K. Segawa, and Y. Ando, Optimizing $Bi_{2-x}Sb_xTe_{3-y}Se_y$ solid solutions to approach the intrinsic topological insulator regime, Phys. Rev. B **84**, 165311 (2011).

[14] N. P. Butch, K. Kirshenbaum, P. Syers, A. B. Sushkov, G. S. Jenkins, H. D. Drew, and J. Paglione, Strong surface scattering in ultrahigh-mobility Bi_2Se_3 topological insulator crystals, Phys. Rev. B **81**, 241301(R) (2010).

[15] T. Arakane, T. Sato, S. Souma, K. Kosaka, K. Nakayama, M. Komatsu, T. Takahashi, Z. Ren, K. Segawa, and Y. Ando, Tunable Dirac cone in the topological insulator $Bi_{2-x}Sb_xTe_{3-y}Se_y$, Nat. Commun. **3**, 636 (2012).

[16] B. Xia, P. Ren, A. Sulaev, P. Liu, S. Q. Shen, and L. Wang, Indications of surface-dominated transport in single crystalline nanoflake devices of topological insulator $Bi_{1.5}Sb_{0.5}Te_{1.8}Se_{1.2}$, Phys. Rev. B **87**, 085442 (2013).

[17] C. S. Tang, B. Xia, X. Q. Zou, S. Chen, H. W. Ou, L. Wang, A. Rusydi, J. X. Zhu, and E. M. Chia, Terahertz conductivity of topological surface states in $Bi_{1.5}Sb_{0.5}Te_{1.8}Se_{1.2}$, Sci. Rep. **3**, 3513 (2013).

[18] Y. Ando, T. Hamasaki, T. Kurokawa, K. Ichiba, F. Yang, M. Novak, S. Sasaki, K. Segawa, Y. Ando, and M. Shiraishi, Electrical detection of the spin polarization due to charge flow in the surface state of the topological insulator $Bi_{1.5}Sb_{0.5}Te_{1.7}Se_{1.3}$, Nano Lett. **14**, 6226 (2014).

[19] Y. Pan, D. Wu, J. R. Angevaare, H. Luigjes, E. Frantzeskakis, N. de Jong, E van Heumen, T. V. Bay, B. Zwartsenberg, Y. K. Huang, M. Snelder, A. Brinkman, M. S. Golden, and A. de Visser, Low carrier concentration crystals of the topological insulator $Bi_{2-x}Sb_xTe_{3-y}Se_y$: A magnetotransport study, New J. Phys. **16**, 123035 (2014).

[20] M. Z. Hasan and C. L. Kane, Colloquium: Topological insulators, Rev. Mod. Phys. **82**, 3045 (2010).

[21] Y. S. Hor, A. J. Williams, J. G. Checkelsky, P. Roushan, J. Seo, Q. Xu, H. W. Zandbergen, A. Yazdani, N. P. Ong, and R. J. Cava, Superconductivity in $Cu_xBi_2Se_3$ and Its Implications for Pairing in the Undoped Topological Insulator, Phys. Rev. Lett. **104**, 057001 (2010).

[22] Z. H. Liu, X. Yao, J. F. Shao, M. Zuo, L. Pi, S. Tan, C. J. Zhang, and Y. H. Zhang, Superconductivity with topological surface state in $Sr_xBi_2Se_3$, J. Am. Chem. Soc. **137**, 10512 (2015).

[23] Y. H. Zhou, X. L. Chen, R. R. Zhang, J. F. Shao, X. F. Wang, C. An, Y. Zhou, C. Y. Park, W. Tong, L. Pi, Z. R. Yang, C. J. Zhang, and Y. H. Zhang, Pressure-induced reemergence of superconductivity in topological insulator $Sr_{0.065}Bi_2Se_3$, Phys. Rev. B **93**, 144514 (2016).

[24] T. He, X. F. Yang, T. Terao, T. Uchiyama, T. Ueno, K. Kobayashi, J. Akimitsu, T. Miyazaki, T. Nishioka, K. Kimura, K. Hayashi, N. Happo, H. Yamaoka, H. Ishii, Y. F. Liao, H. Ota, H. Goto, and Y. Kubozono, Pressure-induced superconductivity in $Ag_xBi_{2-x}Se_3$, Phys. Rev. B **97**, 104503 (2018).

[25] See Supplemental Material at http://link.aps.org/supplemental/10.1103/PhysRevB.100.094525 for supporting information and data pertaining to sample preparation and crystal growth, electronic structure, crystal structure, determination of T_c, $h^* - t$ plots, and theoretical calculation of band dispersion.

[26] M. I. Zargarova, P. K. Babaeva, D. S. Azhdarova, Z. D. Melikova, and S. A. Mekhtieva, A study of the systems $CuInSe_2$−InSe ($SnSe_2$, Bi_2Se_3), Inorg. Mater. **31**, 263 (1995).

[27] M. B. Nielsen, P. Parisiades, S. R. Madsen, and M. Bremholm, High-pressure phase transitions in ordered and disordered Bi_2Te_2Se, Dalton Trans. **44**, 14077 (2015).

[28] J. G. Zhao, Z. H. Yu, Q. Y. Hu, Y. Wang, J. Schneeloch, C. Y. Li, R. D. Zhong, Y. Wang, Z. G. Liu, and G. D. Gu, Structural phase transitions of $(Bi_{1-x}Sb_x)_2(Te_{1-y}Se_y)_3$ compounds under high pressure and the influence of the atomic radius on the compression processes of tetradymites, Phys. Chem. Chem. Phys. **19**, 2207 (2017).

[29] L. Zhu, H. Wang, Y. C. Wang, J. Lv, Y. M. Ma, Q. L. Cui, Y. M. Ma, and G. T. Zou, Substitutional Alloy of Bi and Te at High Pressure, Phys. Rev. Lett. **106**, 145501 (2011).

[30] G. T. Liu, L. Zhu, Y. M. Ma, C. L. Lin, J. Liu, and Y. M. Ma, Stabilization of 9/10-fold structure in bismuth selenide at high pressures, J. Phys. Chem. C **117**, 10045 (2013).

[31] M. Einaga, A. Ohmura, A. Nakayama, F. Ishikawa, Y. Yamada, and S. Nakano, Pressure-induced phase transition of Bi_2Te_3 to a bcc structure, Phys. Rev. B **83**, 092102 (2011).

[32] R. Vilaplana, O. Gomis, F. J. Manjón, A. Segura, E. Pérez-González, P. Rodríguez-Hernández, A. Muñoz, J. González, V. Marín-Borrás, V. Muñoz-Sanjosé, C. Drasar, and V. Kucek, High-pressure vibrational and optical study of Bi_2Te_3, Phys. Rev. B **84**, 104112 (2011).

[33] K. Kirshenbaum, P. S. Syers, A. P. Hope, N. P. Butch, J. R. Jeffries, S. T. Weir, J. J. Hamlin, M. B. Maple, Y. K. Vohra, and J. Paglione, Pressure-Induced Unconventional Superconducting Phase in the Topological Insulator Bi_2Se_3, Phys. Rev. Lett. **111**, 087001 (2013).

[34] J. G. Zhao, H. Z. Liu, L. Ehm, D. W. Dong, Z. Q. Chen, and G. D. Gu, High-pressure phase transitions, amorphization, and crystallization behaviors in Bi_2Se_3, J. Phys.: Condens. Matter **25**, 125602 (2013).

[35] Z. H. Yu, L. Wang, Q. Y. Hu, J. G. Zhao, S. Yan, K. Yang, S. Sinogeikin, G. D. Gu, and H. K. Mao, Structural phase transitions in Bi_2Se_3 under high pressure, Sci. Rep. **5**, 15939 (2015).

[36] R. Vilaplana, D. Santamaría-Pérez, O. Gomis, F. J. Manjón, J. González, A. Segura, A. Muñoz, P. Rodríguez-Hernández, E. Pérez-González, V. Marín-Borrás, V. Muñoz-Sanjose, C. Drasar, and V. Kucek, Structural and vibrational study of Bi_2Se_3 under high pressure, Phys. Rev. B **84**, 184110 (2011).

[37] P. P. Kong, J. L. Zhang, S. J. Zhang, J. Zhu, Q. Q. Liu, R. C. Yu, Z. Fang, C. Q. Jin, W. G. Yang, X. H. Yu, J. L. Zhu, and Y. S. Zhao, Superconductivity of the topological insulator Bi_2Se_3 at high pressure, J. Phys.: Condens. Matter **25**, 362204 (2013).

[38] L. Efthimiopoulos, J. M. Zhang, M. Kucway, C. Park, R. Ewing, and Y. J. Wang, Sb_2Se_3 under pressure, Sci. Rep. **3**, 2665 (2013).

[39] P. P. Kong, F. Sun, L. Y. Xing, J. Zhu, S. J. Zhang, W. M. Li, Q. Q. Liu, X. C. Wang, S. M. Feng, X. H. Yu, J. L. Zhu, R. C. Yu, W. G. Yang, G. Y. Shen, Y. S. Zhao, R. Ahuja, H. K. Mao, and C. Q. Jin, Superconductivity in strong spin orbital coupling compound Sb_2Se_3, Sci. Rep. **4**, 6679 (2014).

[40] Y. M. Ma, G. T. Liu, P. W. Zhu, H. Wang, X. Wang, Q. L. Cui, J. Liu, and Y. M. Ma, Determinations of the high-pressure crystal structures of Sb_2Te_3,J. Phys.: Condens. Matter **24**, 475403 (2012).

[41] J. G. Zhao, H. Z. Liu, L. Ehm, Z. Q. Chen, S. Sinogeikin, Y. S. Zhao, and G. D. Gu, Pressure-induced disordered substitution alloy in Sb_2Te_3, Inorg. Chem. **50**, 11291 (2011).

[42] O. Gomis, R. Vilaplana, F. J. Manjón, P. Rodríguez-Hernández, E. Pérez-González, A. Muñoz, V. Kucek, and C. Drasar, Lattice dynamics of Sb_2Te_3 at high pressures, Phys. Rev. B **84**, 174305 (2011).

[43] S. M. Souza, C. M. Poffo, D. M. Trichês, J. C. de Lima, T. A. Grandi, A. Polian, and M. Gauthier, High pressure monoclinic phases of Sb_2Te_3, Physica B **407**, 3781 (2012).

[44] S. Cai, J. Guo, V. A. Sidorov, Y. Zhou, H. Wang, G. Liu, X. Li, Y. Li, K. Yang, A. Li, Q. Wu, J. Hu, S. K. Kushwaha, R. J.

Cava, and L. Sun, Independence of topological surface state and bulk conductance in three-dimensional topological insulators, npj Quantum Mater. **3**, 62 (2018).

[45] J.-S. Kim, R. Juneja, N. P. Salke, W. Palosz, V. Swaminathan, S. Trivedi, A. K. Singh, D. Akinwande, and J.-F. Lin, Structural, vibrational, and electronic topological transitions of $Bi_{1.5}Sb_{0.5}Te_{1.8}Se_{1.2}$ under pressure, J. Appl. Phys. **123**, 115903 (2018).

[46] J. L. Zhang, S. J. Zhang, H. M. Weng, W. Zhang, L. X. Yang, Q. Q. Liu, S. M. Feng, X. C. Wang, R. C. Yu, L. Z. Cao, L. Wang, W. G. Yang, H. Z. Liu, W. Y. Zhao, S. C. Zhang, X. Dai, Z. Fang, and C. Q. Jin, Pressure-induced superconductivity in topological parent compound Bi_2Te_3, Proc. Natl. Acad. Soc. USA **108**, 24 (2011).

[47] N. R. Werthamer, E. Helfand, and P. C. Hohenberg, Temperature and purity dependence of the superconducting critical field, H_{c2}. III. Electron spin and spin-orbit effects, Phys. Rev. **147**, 295 (1966).

[48] K. Scharnberg and R. A. Klemm, *P*-wave superconductors in magnetic fields, Phys. Rev. B **22**, 5233 (1980).

[49] E. Helfand and N. R. Werthamer, Temperature and purity dependence of the superconducting critical field, H_{c2}. II, Phys. Rev. **147**, 288 (1966).

[50] K. Maki, E. Puchkaryov, G. F. Wang, and H. Won, Aspects of *p*-wave superconductivity, Chin. J. Phys. (Taipei) **38**, 386 (2000).

[51] K. Koepernik and H. Eschrig, Full-potential non-orthogonal local-orbital minimum-basis band-structure scheme, Phys. Rev. B **59**, 1743 (1999).

[52] J. P. Perdew, K. Burke, and M. Ernzerhof, Generalized Gradient Approximation Made Simple, Phys. Rev. Lett. **77**, 3865 (1996).